Supporting Information: Elucidating Ultranarrow $^2F_{7/2}$ to $^2F_{5/2}$ Absorption in Ytterbium(III) Complexes

Barry Y. Li,[1] Claire E. Dickerson,[1] Ashley J. Shin,[1] Changling Zhao,[2] Yi Shen,[1] Yongjia He,[1] Paula L. Diaconescu,[1] Anastassia N. Alexandrova,[1,3] and Justin R. Caram[1]

[1]*Department of Chemistry and Biochemistry, University of California, Los Angeles, California, 90095, USA*
[2]*Department of Physics and Astronomy, University of California, Los Angeles, California, 90095, USA*
[3]*Department of Materials Science and Engineering, University of California, Los Angeles, California, 90095, USA*

Contents

1. Spin-orbit and crystal field effects acting on 4f orbitals

First, to simplify the calculation, we model Yb(III) as a one-hole ($[Xe]4f^{13}$) system, i.e., we ignore as many electron-electron interactions as possible to start by constructing 14 degenerate hydrogen-like $|m_l\, m_s\rangle$ basis with $m_l = -3, -2, \ldots, 1, 2, 3$, and $m_s = \pm 1/2$.[1,2] The components of the total Hamiltonian operator are $\hat{H} = \hat{H}_0 + \hat{H}_{SO} + \hat{H}_{CF}$, where $\hat{H}_0$ is the generic hydrogen-atom Hamiltonian with kinetic and electron-nuclear potential, $\hat{H}_{SO}$ is the spin-orbit interaction, and $\hat{H}_{CF}$ accounts for the crystal field perturbation. For the spin-orbit term,

$$\hat{H}_{SO} \approx \xi_{Yb}^{4f}\, \hat{l} \cdot \hat{s}, \qquad \text{(eq. S1)}$$

where ξ_{Yb}^{4f} is one-electron spin-orbit coupling parameter ($\sim 2{,}870$ cm^{-1}) for Yb(III), $\hat{l} \cdot \hat{s}$ is the dot product of the orbital and spin angular momentum operators. The matrix elements, $\langle m_l\, m_s|\, \hat{l} \cdot \hat{s}\, |m_l'\, m_s'\rangle$ for 4f systems can therefore be obtained from the hydrogen-like angular functions. Without crystal field splitting ($\hat{H}_{CF} = 0$), we can diagonalize this matrix and obtain the angular-momentum-coupled $|j\, m_j\rangle$ representations, which have 8 degenerate ground states with $j = \frac{7}{2}$ and with a $-\frac{3}{2}\xi_{Yb}^{4f}$ energy shift, and 6 excited states with $j = \frac{5}{2}$ with a $+2\xi_{Yb}^{4f}$ energy shift, these states are often labeled according to their term symbols $^2F_{7/2}$ and $^2F_{5/2}$.[1]

$\lvert j\, m_j\rangle$	$\lvert m_l\, m_s\rangle$	Energies
$\left\lvert \frac{5}{2} \pm \frac{1}{2}\right\rangle$	$\mp\sqrt{4/7}\left\lvert \pm 1 \mp \frac{1}{2}\right\rangle \pm \sqrt{3/7}\left\lvert 0 \pm \frac{1}{2}\right\rangle$	
$\left\lvert \frac{5}{2} \pm \frac{3}{2}\right\rangle$	$\mp\sqrt{5/7}\left\lvert \pm 2 \mp \frac{1}{2}\right\rangle \pm \sqrt{2/7}\left\lvert \pm 1 \pm \frac{1}{2}\right\rangle$	$+2\xi_{Yb}^{4f}$
$\left\lvert \frac{5}{2} \pm \frac{5}{2}\right\rangle$	$\mp\sqrt{6/7}\left\lvert \pm 3 \mp \frac{1}{2}\right\rangle \pm \sqrt{1/7}\left\lvert \pm 2 \pm \frac{1}{2}\right\rangle$	
$\left\lvert \frac{7}{2} \pm \frac{1}{2}\right\rangle$	$\sqrt{3/7}\left\lvert \pm 1 \mp \frac{1}{2}\right\rangle + \sqrt{4/7}\left\lvert 0 \pm \frac{1}{2}\right\rangle$	
$\left\lvert \frac{7}{2} \pm \frac{3}{2}\right\rangle$	$\sqrt{2/7}\left\lvert \pm 2 \mp \frac{1}{2}\right\rangle + \sqrt{5/7}\left\lvert \pm 1 \pm \frac{1}{2}\right\rangle$	$-\frac{3}{2}\xi_{Yb}^{4f}$
$\left\lvert \frac{7}{2} \pm \frac{5}{2}\right\rangle$	$\sqrt{1/7}\left\lvert \pm 3 \mp \frac{1}{2}\right\rangle + \sqrt{6/7}\left\lvert \pm 2 \pm \frac{1}{2}\right\rangle$	
$\left\lvert \frac{7}{2} \pm \frac{7}{2}\right\rangle$	$\left\lvert \pm 3 \pm \frac{1}{2}\right\rangle$	

Table S1. Eigenfunctions with eigenvalues of Yb(III) free ion, with angular momenta-coupled and uncoupled basis.

Here the $|m_l\, m_s\rangle$ functions are ordered as $\left\lvert +3\ +\frac{1}{2}\right\rangle$, $\left\lvert +2\ +\frac{1}{2}\right\rangle$, $\left\lvert +1\ +\frac{1}{2}\right\rangle$, $\left\lvert 0\ +\frac{1}{2}\right\rangle$, $\left\lvert -1\ +\frac{1}{2}\right\rangle$, $\left\lvert -2\ +\frac{1}{2}\right\rangle$, $\left\lvert -3\ +\frac{1}{2}\right\rangle$, $\left\lvert +3\ -\frac{1}{2}\right\rangle$, $\left\lvert +2\ -\frac{1}{2}\right\rangle$, $\left\lvert +1\ -\frac{1}{2}\right\rangle$, $\left\lvert 0\ -\frac{1}{2}\right\rangle$, $\left\lvert -1\ -\frac{1}{2}\right\rangle$, $\left\lvert -2\ -\frac{1}{2}\right\rangle$, $\left\lvert -3\ -\frac{1}{2}\right\rangle$.

The crystal field Hamiltonian ($\hat{H}_{CF}$) can be obtained by applying the following operator to the $|m_l\rangle$ basis states (with no spin) for all 7 4f orbitals:[3–5]

$$\hat{H}_{CF} = \sum_{k=1}^{k_{max}} \sum_{-k}^{+k} B_q^k C_q^k, \qquad \text{(eq. S2)}$$

where C_q^k is the associated Racah tensor, B_q^k is the crystal field parameter, k and q are Racah tensor indices, $k_{max} = 6$ for the f-subshell. The crystal field parameter, $B_q^k \approx A_q^k \langle r^k \rangle$, where $\langle r^k \rangle$ denotes the kth moment integral of the radial function and A_q^k are the geometric coordination factors, which can be derived from a point-charge model:

$$A_q^k = \frac{e^2}{4\pi\varepsilon_0} \sum_{i=1}^{N} \frac{(-1)^q Q_i C_{-q}^k (\theta_i, \phi_i)}{R_i^{k+1}}, \qquad \text{(eq. S3)}$$

$e^2/4\pi\varepsilon_0$ is the typical Coulomb term, Q_i is the charge of the Yb center of the ith ligand, (θ_i, ϕ_i) are the polar angles of the ith point charge that corresponds to the Yb-coordinating atom of the ligand, R_i is the radial distance from the ith ligand to the central (Yb) atom, and N is the total number of ligands.[4,6] Thus, the crystal field perturbation is approximated from the electric field generated by the local charges associated with each ligand group. To perform the initial charge assignment to these dative-bonded atoms, according to -1/4 of the complete Pauling's electronegativity, for example, F is assigned a value of -1e, and O is assigned as -0.875e, then normalize them to make sure the sum is -3. If there are more than 6 coordination sites, some of them can be grouped according to the ligand positions, and an effective charge is estimated. If there are fewer than 6 coordination sites, assign 0 as a placeholder. Next, perform the initial rigid rotational scanning to find the position with the smallest energy deviation (Section 4, SI) and then perform random sampling on the charge at the best position obtained by the rotation, allowing ones with the initial value (-1/4 of the Pauling's complete electronegativity) less than or equal to -0.625e (carbon standard) to continue to become smaller until it tends to -1e, and other ones with the value greater than -0.625e continue to increase until it tends to 0, the best energy deviation from the experimental data is screened to determine the charge distribution.

It is worth mentioning that this step can be replaced by a much higher-level computation, such as CASSCF (complete active space self-consistent field) with the LoProp method to define the point charges. With the local-charge treatment, the calculated crystal field parameters are tabulated in Table S2 – S5 for different structures.

As Yb(III) has a relatively large spin-orbit coupling further modified by crystal field splitting, in order to determine the energies, wave functions, and oscillator strengths of these transitions, it is necessary to evaluate the total perturbation Hamiltonian in one step. This approach differs from the application of crystal field splitting followed by perturbation of spin-orbit coupling, as typically done for transition metal complexes.[7] The total perturbation Hamiltonian is therefore $(\hat{H}_{SO} + \hat{H}_{CF})$, this can be constructed by a simple matrix addition of the spin-orbit Hamiltonian matrix and the augmented crystal field Hamiltonian matrix. To augment the matrix, one can diagonally input 2 identical 7×7 spin-free crystal field matrices, the total Hamiltonian is then:[8,9]

$$H_{SOCF} = \xi_{Yb}^{4f} \begin{bmatrix} \ddots & \vdots & \cdots \\ \cdots & \langle i | \hat{l} \cdot \hat{s} | j \rangle & \cdots \\ \cdots & \vdots & \ddots \end{bmatrix} + \begin{bmatrix} [H_{CF}^{spin-free}] & 0 \\ 0 & [H_{CF}^{spin-free}] \end{bmatrix}. \qquad \text{(eq. S4)}$$

In general, the diagonalization of this perturbation Hamiltonian results in 4 pairs of closely spaced electron configurations near the ground state and 3 pairs on the excited state, depending on the crystal field anisotropy.

k	q	Re[$4f\,B_q^k$] (cm^{-1})	Im[$4f\,B_q^k$] (cm^{-1})	Re[$5d\,B_q^k$] (cm^{-1})	Im[$5d\,B_q^k$] (cm^{-1})
1	0	-66.5081	0.0000	11.9432	0.0000
1	1	796.0440	1010.6760	-142.9500	-181.4927
2	0	-40.1381	0.0000	7.5777	0.0000
2	1	-499.1851	435.6369	94.2414	-82.2441
2	2	202.0431	-941.8736	-38.1438	177.8168
3	0	42.4566	0.0000	-3.3800	0.0000
3	1	-199.5593	-269.8056	15.8870	21.4793
3	2	-165.4582	-69.6043	13.1722	5.5412
3	3	-197.5260	82.1040	15.7251	-6.5363
4	0	0.3960	0.0000	0.0842	0.0000
4	1	-19.4251	13.2985	-4.1328	2.8293
4	2	-4.5461	20.0596	-0.9672	4.2678
4	3	-15.9277	-26.4550	-3.3887	-5.6284
4	4	35.4802	16.3659	7.5485	3.4819
5	0	-1.1265	0.0000		
5	1	4.0711	3.9051		
5	2	-8.0592	-1.0296		
5	3	3.1929	-2.1116		
5	4	1.6007	-1.2151		
5	5	-1.8324	-9.8326		
6	0	2.6510	0.0000		
6	1	0.8258	0.0607		
6	2	0.7256	-1.9376		
6	3	-0.2403	-1.6914		
6	4	-2.2053	-1.3541		
6	5	-0.4861	-0.2568		
6	6	-1.2921	1.4645		

Table S2. Real and imaginary part of the crystal filed parameters for $4f$ and $5d$ orbitals in YbCp$_3$.

k	q	Re[$4f\,B_q^k$] (cm^{-1})	Im[$4f\,B_q^k$] (cm^{-1})	Re[$5d\,B_q^k$] (cm^{-1})	Im[$5d\,B_q^k$] (cm^{-1})
1	0	6644.7499	0.0000	-1193.2344	0.0000
1	1	-5231.5719	1324.3382	939.4622	-237.8187
2	0	277.5078	0.0000	-52.3908	0.0000
2	1	-605.2604	420.0377	114.2674	-79.2991
2	2	485.2322	-168.7346	-91.6072	31.8555
3	0	-89.8452	0.0000	7.1526	0.0000
3	1	47.0696	52.3076	-3.7472	-4.1642
3	2	-365.1364	379.3659	29.0686	-30.2015
3	3	48.5752	175.4990	-3.8671	-13.9715
4	0	70.9590	0.0000	15.0968	0.0000
4	1	17.1031	-44.1930	3.6387	-9.4022
4	2	45.3621	-38.1363	9.6510	-8.1137
4	3	-23.2486	31.5376	-4.9462	6.7098
4	4	6.7770	65.7480	1.4418	13.9882
5	0	-10.0671	0.0000		
5	1	5.8665	2.3041		
5	2	2.3977	-4.0421		
5	3	0.2175	2.7266		
5	4	4.7702	-7.3096		
5	5	1.3344	5.1182		
6	0	-3.1248	0.0000		
6	1	-0.5740	0.9056		
6	2	-0.9065	0.4767		
6	3	1.3625	-0.5125		
6	4	-0.1038	5.1016		
6	5	3.0940	0.8922		
6	6	0.5471	-0.7597		

Table S3. Real and imaginary part of the crystal filed parameters for $4f$ and $5d$ orbitals in K$_3$[Yb(BINOL)$_3$].

k	q	Re[$4f\ B_q^k$] (cm⁻¹)	Im[$4f\ B_q^k$] (cm⁻¹)	Re[$5d\ B_q^k$] (cm⁻¹)	Im[$5d\ B_q^k$] (cm⁻¹)
1	0	-4177.1706	0.0000	750.1176	0.0000
1	1	-3928.0095	-4952.0527	705.3743	889.2674
2	0	-206.2645	0.0000	38.9408	0.0000
2	1	513.1783	497.2677	-96.8832	-93.8794
2	2	-133.3239	464.4334	25.1703	-87.6806
3	0	-497.2691	0.0000	39.5878	0.0000
3	1	257.7402	0.1434	-20.5188	-0.0114
3	2	-121.2209	-26.6320	9.6504	2.1202
3	3	-224.9064	229.5616	17.9049	-18.2755
4	0	-95.2630	0.0000	-20.2676	0.0000
4	1	26.1608	-42.2139	5.5658	-8.9812
4	2	17.5688	-3.8112	3.7378	-0.8108
4	3	19.2769	-38.1360	4.1012	-8.1136
4	4	-69.6630	9.0460	-14.8211	1.9246
5	0	-3.3208	0.0000		
5	1	3.3439	0.7560		
5	2	1.1895	3.8918		
5	3	6.4234	-2.5523		
5	4	10.1574	1.9756		
5	5	-3.8118	0.0692		
6	0	-2.6971	0.0000		
6	1	3.4304	0.2639		
6	2	-3.2092	0.7866		
6	3	-1.0479	1.7133		
6	4	1.0730	-0.9961		
6	5	-0.4818	1.4419		
6	6	-0.2645	2.6437		

Table S4. Real and imaginary part of the crystal filed parameters for $4f$ and $5d$ orbitals in Yb(trensal).

k	q	Re[$4f\ B_q^k$] (cm⁻¹)	Im[$4f\ B_q^k$] (cm⁻¹)	Re[$5d\ B_q^k$] (cm⁻¹)	Im[$5d\ B_q^k$] (cm⁻¹)
1	0	2901.5040	0.0000	-521.0391	0.0000
1	1	-1942.3946	-516.8870	348.8065	92.8202
2	0	1881.9687	0.0000	-355.2978	0.0000
2	1	-482.1067	-382.5983	91.0172	72.2309
2	2	-177.8356	40.6583	33.5737	-7.6759
3	0	-102.2841	0.0000	8.1429	0.0000
3	1	148.9407	16.4918	-11.8572	-1.3129
3	2	111.3184	43.3571	-8.8621	-3.4517
3	3	104.0362	-20.1471	-8.2824	1.6039
4	0	-41.4641	0.0000	-8.8217	0.0000
4	1	15.3120	21.1899	3.2577	4.5082
4	2	-12.3705	-9.4796	-2.6319	-2.0168
4	3	-31.9933	-15.4721	-6.8067	-3.2917
4	4	-0.0467	-89.1075	-0.0099	-18.9580
5	0	2.8006	0.0000		
5	1	-9.8100	-1.7266		
5	2	-3.4334	-0.8046		
5	3	0.9374	5.9362		
5	4	1.9284	5.3598		
5	5	5.0865	-7.9369		
6	0	1.1586	0.0000		
6	1	0.1125	-0.9673		
6	2	1.1600	0.7257		
6	3	1.3363	0.2210		
6	4	-0.9941	1.7658		
6	5	0.2294	-1.2749		
6	6	-0.1724	-0.8617		

Table S5. Real and imaginary part of the crystal filed parameters for $4f$ and $5d$ orbitals in (thiolfan)YbCl(THF).

2. Magnetic dipole (M1) transition oscillator strength

If we only consider 4f orbitals, f-f transitions have no change in orbital angular momentum quantum number ($\Delta l = 0$). This implies that transitions between different electron configurations are electric dipole (E1) forbidden. The first order transition that is allowed is via magnetic dipole transition (M1). We will compute the magnetic dipole oscillator strength M1 with the magnetic dipole moment operator, $\widehat{M}$:[10]

$$M1_{f\leftarrow i} = \frac{2m_e(E_f - E_i)}{3\hbar^2 e^2 c^2}\frac{n_r}{g_1}\left|\langle f|\widehat{M}|i\rangle\right|^2. \tag{eq. S5}$$

where i indicates the initial state, f indicates the final state, e is the elementary charge, m_e is the electron rest mass, c denotes the speed of light in vacuum, n_r is the index of refraction of the sample, and where g_1 is the degeneracy of the initial lower states.[11] Further,

$$M1_{f\leftarrow i} = \frac{2m_e(E_f - E_i)}{3\hbar^2 e^2 c^2}\frac{n_r}{g_1}\left|\langle f|\widehat{M}_x\boldsymbol{i} + \widehat{M}_y\boldsymbol{j} + \widehat{M}_z\boldsymbol{k}|i\rangle\right|^2, \tag{eq. S6}$$

where

$$\widehat{M}_z = -\frac{\mu_B}{\hbar}\sum_i\left(\hat{l}_z + 2\hat{s}_z\right)_i, \tag{eq. S7}$$

$$\widehat{M}_x = -\frac{\mu_B}{\hbar}\sum_i\left(\hat{l}_x + 2\hat{s}_x\right)_i, \tag{eq. S8}$$

$$\widehat{M}_y = -\frac{\mu_B}{\hbar}\sum_i\left(\hat{l}_y + 2\hat{s}_y\right)_i. \tag{eq. S9}$$

Since

$$\hat{l}_x = \frac{1}{2}\left(\hat{l}_+ + \hat{l}_-\right), \tag{eq. S10}$$

$$\hat{l}_y = \frac{1}{2i}\left(\hat{l}_+ - \hat{l}_-\right), \tag{eq. S11}$$

$$\hat{s}_x = \frac{1}{2}\left(\hat{s}_+ + \hat{s}_-\right), \tag{eq. S12}$$

$$\hat{s}_y = \frac{1}{2i}\left(\hat{s}_+ - \hat{s}_-\right), \tag{eq. S13}$$

operators $\widehat{M}_x$ and $\widehat{M}_y$ are therefore[12]

$$\widehat{M}_x = -\frac{\mu_B}{2\hbar}\sum_i\left(\hat{l}_+ + \hat{l}_- + 2\hat{S}_+ + 2\hat{S}_-\right)_i, \tag{eq. S14}$$

$$\widehat{M}_y = -\frac{\mu_B}{2i\hbar}\sum_i\left(\hat{l}_+ - \hat{l}_- + 2\hat{S}_+ - 2\hat{S}_-\right)_i. \tag{eq. S15}$$

3. Judd-Ofelt treatment of 5d mixing and electric dipole (E1) transition

In the 1950s, it was recognized that the M1 oscillator strength was not enough to account for the apparent absorption of rare earths in crystals.[13] To explain these results, it was suggested that the transition must have an E1 character, which implies mixing of orbitals of different parity. This was formalized as the Judd-Ofelt theory, where nearby unoccupied orbitals (e.g., 5d states) mix with the 4f active space, enabled by an anisotropic crystal field perturbation.[14–17]

After the SOCF calculation using the 4f-only framework, a total number of 14 different SOCF states are obtained (denoted as $|\psi_{4f}^{SOCF}\rangle$) with associated energy E_{4f}^{SOCF}, where each state is just the linear combinations of the 14 distinct 4f states in the $|m_l\ m_s\rangle$ basis. The 5d states, which carry even parity, are represented as $|\psi_{5d}\rangle$. Since the 5d ($l = 2$) spin-orbit coupling is assumed much smaller than the 4f ($l = 3$) states, it is neglected for simplicity. The overall normalized 5d-admixed states, $|\eta_i\rangle$ with its complex conjugate $\langle\eta_i|$ are[18–21]

$$|\eta_i\rangle = N_i\left(|\psi_{4f,i}^{SOCF}\rangle + \sum_{j=1}^{10}\frac{\langle\psi_{4f,i}^{SOCF}|\widehat{H}_{LF}|\psi_{5d,j}\rangle}{E_{4f}^{SOCF} - E_{5d}}|\psi_{5d,j}\rangle\right), \qquad \text{(eq. S16)}$$

$$\langle\eta_i| = N_i'\left(\langle\psi_{4f,i}^{SOCF}| + \sum_{j=1}^{10}\frac{\langle\psi_{4f,i}^{SOCF}|\widehat{H}_{LF}|\psi_{5d,j}\rangle}{E_{5d} - E_{4f}^{SOCF}}\langle\psi_{5d,j}|\right). \qquad \text{(eq. S17)}$$

The energy denominator in the conventional Judd-Ofelt theory is typically determined by fitting the relative intensity of electronic transitions between different spin-orbit states in the absorption spectra of lanthanides. However, Yb(III) has only one spin-orbit transition, leading to an under-prescribed fit. For a reasonable approximation of the energy denominator, we subtract the energy of the 5d orbitals from the eigen energies associated with the parity-unmixed states through the 4f-only SOCF calculation. After the parity mixing, the electric dipole (E1) transitions are now allowed, and the E1 oscillator strength is calculated with the electric dipole operator, $\widehat{\boldsymbol{\mu}}$, as follows:[10]

$$E1_{f\leftarrow i} = \frac{2m_e\left(E_f - E_i\right)}{3\hbar^2 e^2}\frac{n_r}{g_1}|\langle f|\widehat{\boldsymbol{\mu}}|i\rangle|^2. \qquad \text{(eq. 18)}$$

Where i and f denote the final and initial states.

Since obtaining the precise energy of the 5d states is challenging, we conduct a scan across different 5d energy values until the magnitude of absolute oscillator strengths closely matches the experimentally observed values. First of all, compared to the energy of 4f (no spin-orbit, no crystal field), 5d should not exceed the 5d energy of hydrogen-like atoms (~ 9 eV higher than 4f), nor should it be lower than the gas-phase spin-orbit excited 4f band (~ 0.72 eV above 4f). The overall dipole-approximated oscillator strength of M1+E1 can be calculated based on point charges, and sample through different 5d/4f gaps within the range to find one that provides the oscillator strength closest to 10^{-6}.[22,23]
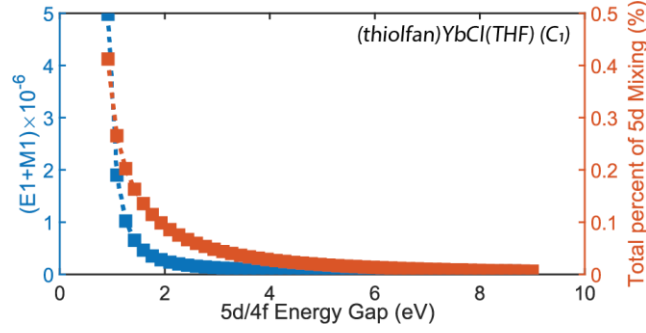
Figure S1. Illustration of the dipole approximated oscillator strength (E1+M1) and the total percent of 5d mixing (into the 4f manifold) vs. the 5d/4f gap, the desired 10^{-6} oscillator strength occurs around the 1 eV 5d/4f energy gap.

Also, with the treatment of Judd-Ofelt theory, the percent of 5d mixing for each SOCF state can be obtained as

$$5d\%_i = 100\% \times N_i^2 \sum_{j=1}^{10} \left| \frac{\langle \psi_{5d,j} | \hat{H}_{LF} | \psi_{4f,i}^{SOCF} \rangle}{E_{4f}^{SOCF} - E_{5d}} \right|^2. \qquad \text{(eq. S19)}$$

4. 3-Stage fitting mechanism (rigid-bond rotation and charge samplings)

The fitting is accomplished by multiple single-pint SOCF calculations, where the 3-stage fitting mechanism is applied, as illustrated in Figure S2. Based on the initial charge orientation from the inner-coordination-sphere atomic positions, with the initial assigned charges based on electronegativity, the first stage is a crude rigid-bond rotation, where about only 72 points are scanned with multiple drop-down latitudes and the azimuthal longitudes covering the whole sphere as shown in Figure S2. Next, a random charge sampling with 200 points is applied to the best fit from the crude scan, which allows ones with the initial value (-1/4 of the Pauling's complete electronegativity) less than or equal to -0.625 (carbon standard) to continue to become smaller until it tends to -1, and other ones with the value greater than -0.625 continue to increase until it tends to 0, where they are both set to space 10° (fine to 360° (initial scan). First, the rotational operation is controlled by the rotation matrix along z axis, or the ϕ rotation, azimuthal longitudes,

$$R_z(\phi) = \begin{bmatrix} \cos\phi & -\sin\phi & 0 \\ \sin\phi & \cos\phi & 0 \\ 0 & 0 & 1 \end{bmatrix}. \qquad \text{(eq. S20)}$$

Then, for each longitude, the drop-down rotations are performed for the latitude scan, this rotation is controlled by the rotation matrix along x axis,

$$R_x(\theta) = \begin{bmatrix} 1 & 0 & 0 \\ 0 & \cos\theta & -\sin\theta \\ 0 & \sin\theta & \cos\theta \end{bmatrix}. \qquad \text{(eq. S21)}$$

In the initial scan, only four transition energies are considering, where in the fine rotation, all fitting parameters are considered, i.e., the transition oscillator strengths are included. The percent error is used as the optimization parameter for the fitting, where

$$\text{error \%} \equiv \frac{1}{n}\sum_n \frac{|\text{calculated}_n - \text{experimental}_n|}{\text{experimental}_n} \times 100.$$

(eq. S22)

To understand how sensitive the percent errors respond to the change of ϕ and θ (in degree), the Hessians are calculated for four Yb(III) complexes studied, they are denoted as $D_{\phi\phi}$, $D_{\phi\theta}$, and $D_{\theta\theta}$, assuming $D_{\phi\theta} = D_{\theta\phi}$, where

$$\text{Hessian}(D) = \begin{bmatrix} \dfrac{\partial^2}{\partial\phi^2} & \dfrac{\partial^2}{\partial\phi\partial\phi} \\ \dfrac{\partial^2}{\partial\theta\partial\phi} & \dfrac{\partial^2}{\partial\theta^2} \end{bmatrix}(\text{error \%}).$$
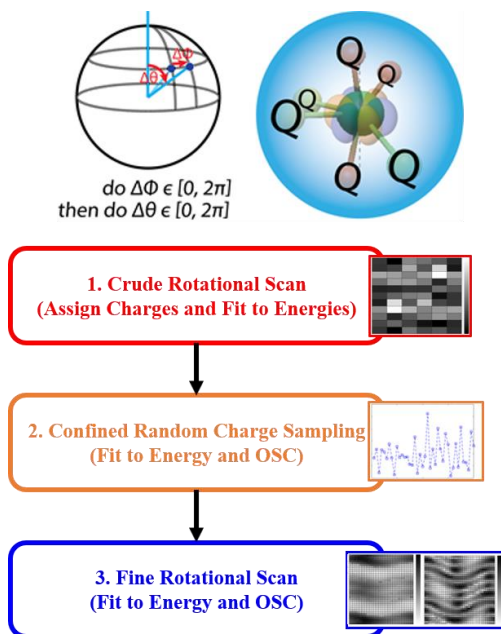
(eq. S23)

Figure S2. Schematic illustration of the 3-stage fitting mechanism. The crude scan takes the initial charges (as described in section 1) and rotates along *z*-axis first and then *x*-axis, using only ~ 72 points to find the optimal position of charges fitting to the transition energies. The second step is to randomly sample effective charge values with confinements to get the optimal fitting to the transition energies and oscillator strengths. Finally, a fine rotational scan is performed with > 256 points to find the optimal position to best fit the transition energies and oscillator strengths.

	Crude Scan Error	Charge Sample	Fine Scan E1+M1	Fine Scan Error
YbCp₃				
			Best Fit: $\Delta\phi = 30°$ and then $\Delta\theta = 60°$.	
K₃[Yb(BINOL)₃]				
			Best Fit: $\Delta\phi = 150°$ and then $\Delta\theta = 210°$.	
Yb(trensal)				
			Best Fit: $\Delta\phi = 180°$ and then $\Delta\theta = 90°$.	
(thiolfan)YbCl(THF)				
			Best Fit: $\Delta\phi = 80°$ and then $\Delta\theta = 170°$.	

Table S6. Results of the 3-stage fitting mechanism for four complexes discussed in this work.

Charge #	x (Å)	y (Å)	z (Å)	Local Charge (e)
1	0.0000	0.0000	0.0000	+3.0000
2	-0.8985	1.1406	0.0529	-0.9004
3	1.0220	-0.2880	1.2321	-0.9004
4	-0.0161	-0.9889	-1.2913	-0.9004
5	-1.4678	-1.1997	0.9369	0.0000
6	-1.4678	-1.1997	0.9369	-0.1494
7	1.4677	1.1997	-0.9369	-0.1494

Table S7. Final optimal effective charges and their Cartesian coordinates for YbCp₃ obtained from the 3-stage fitting mechanism.

Charge #	x (Å)	y (Å)	z (Å)	Local Charge (e)
1	0.0000	0.0000	0.0000	+3.0000
2	1.1655	0.6107	0.5738	-0.9226
3	-0.3721	1.0132	-1.0087	-0.9226
4	0.4300	-1.0947	-0.7343	-0.9226
5	-2.2593	-0.7582	-0.1687	-0.0774
6	-0.2059	-1.3285	1.9842	-0.0774
7	-1.2789	1.5154	1.5763	-0.0774

Table S8. Final optimal effective charges and their Cartesian coordinates for K₃[Yb(BINOL)₃] obtained from the 3-stage fitting mechanism.

Charge #	x (Å)	y (Å)	z (Å)	Local Charge (e)
1	0.0000	0.0000	0.0000	+3.0000
2	1.4149	0.1913	-0.1235	-0.8989
3	-0.1316	-1.3388	-0.4939	-0.8989
4	-0.2947	-0.0916	1.3994	-0.8989
5	-2.3763	0.2379	-0.4983	-0.1011
6	-0.2621	2.4253	0.0348	-0.1011
7	-0.0552	0.5850	-2.3678	-0.1011

Table S9. Final optimal effective charges and their Cartesian coordinates for Yb(trensal) obtained from the 3-stage fitting mechanism.

Charge #	x (Å)	y (Å)	z (Å)	Local Charge (e)	CAS Charge (e)
1	0.0000	0.0000	0.0000	+3.0000	+3.0000
2	1.4348	0.8262	0.9240	-0.7046	-0.6152
3	1.0895	-1.8056	-0.2398	-0.6886	-0.6510
4	-1.3784	1.4259	0.1222	-0.7600	-0.7496
5	-1.5085	-1.2469	-0.1051	-0.7321	-0.7520
6	1.4969	0.8908	-2.4338	-0.0421	-0.1122
7	0.5410	-0.7578	2.4844	-0.0726	-0.1193

Table S10. Final optimal effective charges and their Cartesian coordinates for (thiolfan)YbCl(THF) obtained from the 3-stage fitting mechanism. The last column shows the local charge information (CAS Charge) approximated from the LoProp charge calculation based on SOC-CASSCF/RASSI theory.
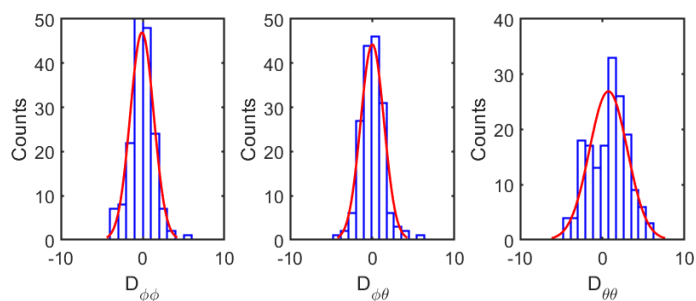
Figure S3. Histograms of deviation Hessian matrix elements for YbCp$_3$. Gaussian full width at half maximum: $FWHM(D_{\phi\phi}) = 3.3814$, $FWHM(D_{\phi\theta}) = 3.3375$, and $FWHM(D_{\theta\theta}) = 5.4278$.
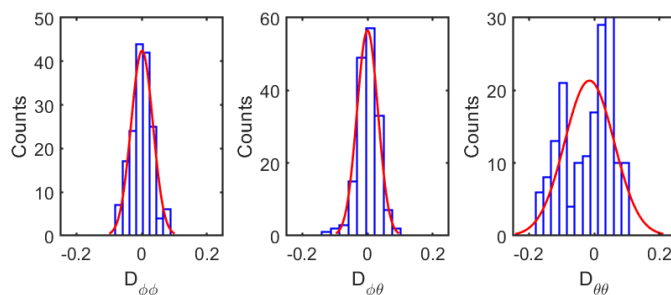

Figure S4. Histograms of deviation Hessian matrix elements for K$_3$[Yb(BINOL)$_3$]. Gaussian full width at half maximum: $FWHM(D_{\phi\phi}) = 0.078622$, $FWHM(D_{\phi\theta}) = 0.075883$, and $FWHM(D_{\theta\theta}) = 0.17851$.
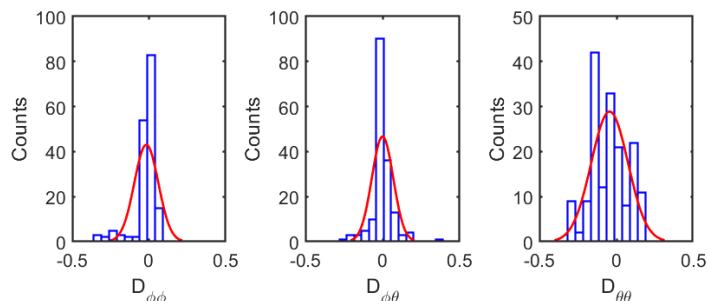

Figure S5. Histograms of deviation Hessian matrix elements for Yb(trensal). Gaussian full width at half maximum: $FWHM(D_{\phi\phi}) = 0.18450$, $FWHM(D_{\phi\theta}) = 0.16327$, and $FWHM(D_{\theta\theta}) = 0.28022$.
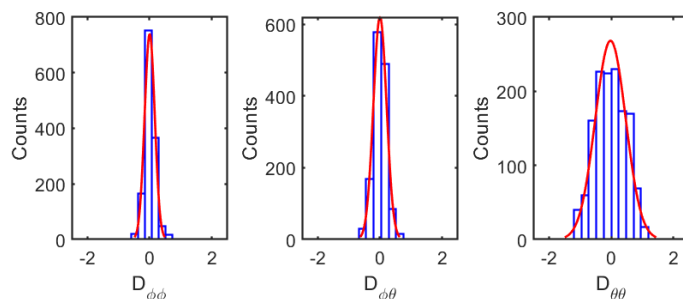

Figure S6. Histograms of deviation Hessian matrix elements for (thiolfan)YbCl(THF). Gaussian full width at half maximum: $FWHM(D_{\phi\phi}) = 0.38287$, $FWHM(D_{\phi\theta}) = 0.49800$, and $FWHM(D_{\theta\theta}) = 1.1507$.

5. Full spectral calculation table

	Initial	Final	Calc. E (eV)	Expt. E (eV)	E1+M1	E1+M1 with k_BT
YbCp₃	1, 2	9, 10	1.2625	1.2603	8.5660E-07	8.5660E-07
		11, 12	1.2701	1.2710	4.1860E-07	4.1860E-07
		13, 14	1.3148	1.3160	1.5551E-06	1.5551E-06
	3, 4	9, 10	1.2579	(1.2751)	1.5330E-07	3.5395E-12
		11, 12	1.2654	(1.2934)	1.2870E-07	2.9716E-12
		13, 14	1.3102	(1.3026)	4.9840E-07	1.1508E-11
	5, 6	9, 10	1.2257		4.0580E-07	3.2775E-44
		11, 12	1.2333		1.6538E-06	1.3357E-43
		13, 14	1.2780		1.4182E-06	1.1454E-43
	7, 8	9, 10	1.2021		2.4430E-07	3.2166E-68
		11, 12	1.2097		1.7649E-06	2.3238E-67
		13, 14	1.2544		1.1470E-06	1.5102E-67
K₃[Yb(BINOL)₃]	1, 2	9, 10	1.2688	1.2681	6.3790E-05	6.3790E-05
		11, 12	1.2870	1.2897	6.5475E-05	6.5475E-05
		13, 14	1.3701	-	3.1995E-05	3.1995E-05
	3, 4	9, 10	1.2599	-	8.5364E-06	6.0501E-06
		11, 12	1.2781	-	2.2912E-05	1.6239E-05
		13, 14	1.3612	1.3615	1.5666E-05	1.1103E-05
	5, 6	9, 10	1.2064	-	3.9569E-05	3.5406E-06
		11, 12	1.2246	-	1.0641E-04	9.5220E-06
		13, 14	1.3076	1.3089	8.8896E-05	7.9544E-06
	7, 8	9, 10	1.1502	(1.3281)	2.6678E-05	2.7044E-07
		11, 12	1.1683		7.4768E-05	7.5795E-07
		13, 14	1.2514		1.2065E-04	1.2231E-06
Yb(trensal)	1, 2	9, 10	1.2707	1.2769	1.5378E-05	1.5378E-05
		11, 12	1.3317	1.3247	6.4042E-06	6.4042E-06
		13, 14	1.3827	1.3734	4.9244E-06	4.9244E-06
	3, 4	9, 10	1.2178	1.2198	4.0809E-06	5.0935E-07
		11, 12	1.2788		8.2069E-06	1.0243E-06
		13, 14	1.3298		6.2652E-06	7.8197E-07
	5, 6	9, 10	1.1908		1.2090E-06	5.2169E-08
		11, 12	1.2518		3.7287E-06	1.6090E-07
		13, 14	1.3028		3.0817E-06	1.3298E-07
	7, 8	9, 10	1.1397		1.4780E-06	8.5442E-09
		11, 12	1.2007		7.2068E-06	4.1662E-08
		13, 14	1.2517		1.3976E-05	8.0794E-08
(thiolfan)YbCl (THF)	1, 2	9, 10	1.2645	1.2650	2.8266E-06	2.8266E-06
		11, 12	1.3427	1.3400	3.4916E-06	3.4916E-06
		13, 14	1.3830	1.3820	1.8063E-06	1.8063E-06
	3, 4	9, 10	1.1985	*1.1940	1.1374E-06	8.8545E-08
		11, 12	1.2766		3.3358E-06	2.5969E-07
		13, 14	1.3169		5.2871E-06	4.1159E-07
	5, 6	9, 10	1.1572		2.7020E-07	4.2572E-09
		11, 12	1.2354		2.1961E-06	3.4601E-08
		13, 14	1.2756		5.3961E-06	8.5020E-08
	7, 8	9, 10	1.1312		9.2500E-08	5.3103E-10
		11, 12	1.2093		6.5590E-07	3.7654E-09
		13, 14	1.2544		1.1470E-06	1.5102E-67

Table S11. Calculated f-f transition data with the experimental energy assignments for YbCp₃ at 5 K, and K₃[Yb(BINOL)₃], Yb(trensal), (thiolfan)YbCl(THF) at 300 K. Number with "*" indicates that it is measured from PL, and numbers in parentheses are ones with no suitable matching from calculated electronic structures.[25–28]

6. Atomic similarity factor γ

First, the basis used overall the spin-orbit crystal field calculation is the fully uncoupled Yb(III) 4f atomic orbitals that can be described in 4 quantum numbers, $n = 4, l = 3, m_l = -3 \ldots + 3$, and $m_s = \pm\frac{1}{2}$, there are 14 of them mutually orthogonal, the spatial projections of them are plotted below in Figure S7.
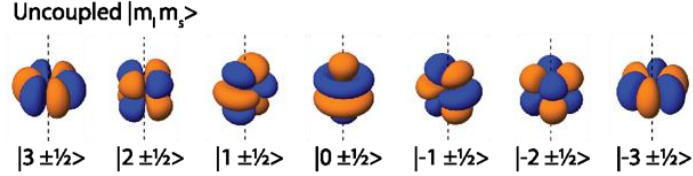

Uncoupled $|m_l m_s\rangle$

$|3 \pm\frac{1}{2}\rangle$ $|2 \pm\frac{1}{2}\rangle$ $|1 \pm\frac{1}{2}\rangle$ $|0 \pm\frac{1}{2}\rangle$ $|-1 \pm\frac{1}{2}\rangle$ $|-2 \pm\frac{1}{2}\rangle$ $|-3 \pm\frac{1}{2}\rangle$

Figure S7. Spatial projection of the uncoupled 14 bare 4f atomic orbitals written in $|m_l m_s\rangle$ basis.

However, this is not the atomic orbitals of interest, the ones that are used to illustrate atomic feature here are the gas-phase states, i.e., spin-orbit coupled (SOC) basis, $|\psi^{SOC}\rangle$, where $n = 4$ and $l = 3$, and the coupled quantum numbers, j and m_j, there are 14 $|j \, m_j\rangle$ states and each can be written in the linear combination of $|m_l \, m_s\rangle$ as tabulated above in Table S1. It is easy to see that these 14 $|j \, m_j\rangle$ states are also mutually orthogonal, and therefore can be used as the atomic/ion basis. In the actual Yb(III) complexes, there are also ligands that bring effects onto the atomic orbitals, which treated as a perturbation of electric field (crystal field) coupling with 5d admixing. Therefore, the normalized resulting states can be written as

$$|\eta\rangle = \sum_{i=1}^{14} c_i^{4f} |m_l \, m_s\rangle_i + c^{5d} \, |5d\rangle, \tag{eq. S24}$$

where the coefficients can be written as a 15-by-1 normalized vector, i.e.,

$$\sum_{i=1}^{14} \left| c_i^{4f} \right|^2 + |c^{5d}|^2 = 1. \tag{eq. S25}$$

Now, to analyze "how similar" the resulting states compare with the gas-phase spin-orbit-only orbitals, a simple overlap is used, and the complex overlap, s, is calculated as

$$s_i = \langle\eta|\psi_i^{SOC}\rangle, \tag{eq. S26}$$

It is important to notice that vector s here is not necessarily normalized, because the SOC states are fully described by a complete basis of $|m_l \, m_s\rangle$, it can only be made normalized by adding back the 5d contribution, i.e.,

$$\sum_{i=1}^{14} |s_i|^2 + |c^{5d}|^2 = 1. \tag{eq. S27}$$

S14

To discuss the atomic similarity, the 15-by-1 overlap amplitude vector, a, is constructed as

$$\langle a_1, a_2, a_3, \dots, a_{14}, a_{15}\rangle = \langle |s_1|^2, |s_2|^2, |s_3|^2, \dots, |s_{14}|^2, |c^{5d}|^2\rangle. \tag{eq. S28}$$

Now, to illustrate how similar the resulting states with the gas-phase SOC states, the Factor of Atomic Similarity, γ, is then defined as the norm-square of a, i.e.

$$\gamma = \sum_{i=1}^{15} |a_i|^2. \tag{eq. S29}$$

There is an upper bound for γ, where a resulting state completely resembles one of the $|\psi^{SOC}\rangle$, i.e., $a = \langle 0,0,0,1,0,0,0,\dots\rangle$, $\gamma|_{max}$ is therefore 1; vice versa, the lower bound of γ indicates the resulting state has absolutely no similarity to any of the specific $|\psi^{SOC}\rangle$, $a = \langle\frac{1}{15}, \frac{1}{15}, \frac{1}{15}, \dots\rangle$, $\gamma|_{min}$ is therefore $15 \times \left(\frac{1}{15}\right)^2 = \frac{1}{15} \approx 0.0667$. For example, the a vector for the State 1 of the (thiolfan)YbCl(THF) and its similarity factor are

$$\langle 0.8549, 0, 0.1366, 0, 0.0072, 0, 0.0006, 0, 0, 0, 0, 0, 0, 0, 0.0007\rangle,$$

$$\gamma_1^{\text{thiolfan}} = 0.7496. \tag{eq. S30}$$

j	State	YbCp₃ (%)	5d%	K₃[Yb(BINOL)₃]	5d%	Yb(trensal)	5d%	(thiolfan)YbCl	5d%
$\frac{5}{2}$	10	29.08 $\lvert+3/2\rangle$ 25.68 $\lvert+1/2\rangle$	0.42	40.13 $\lvert+5/2\rangle$ 31.25 $\lvert+3/2\rangle$	2.78	36.25 $\lvert+3/2\rangle$ 23.62 $\lvert+5/2\rangle$	8.39	90.45 $\lvert-5/2\rangle$ 8.68 $\lvert-3/2\rangle$	0.17
	9	32.67 $\lvert-3/2\rangle$ 27.57 $\lvert-1/2\rangle$	0.80	30.61 $\lvert+3/2\rangle$ 24.80 $\lvert+5/2\rangle$	2.34	36.41 $\lvert-3/2\rangle$ 23.93 $\lvert-5/2\rangle$	10.95	90.64 $\lvert+5/2\rangle$ 8.68 $\lvert+3/2\rangle$	0.18
$\frac{7}{2}$	2	27.14 $\lvert+5/2\rangle$ 24.70 $\lvert+3/2\rangle$	0.01	38.54 $\lvert-5/2\rangle$ 29.78 $\lvert-7/2\rangle$	2.90	32.67 $\lvert+5/2\rangle$ 29.44 $\lvert+3/2\rangle$	0.71	85.91 $\lvert-7/2\rangle$ 11.60 $\lvert-5/2\rangle$	0.04
	1	27.23 $\lvert-3/2\rangle$ 24.66 $\lvert-5/2\rangle$	0.02	39.45 $\lvert+5/2\rangle$ 32.07 $\lvert+7/2\rangle$	2.08	32.66 $\lvert-5/2\rangle$ 30.02 $\lvert-3/2\rangle$	0.68	87.48 $\lvert+7/2\rangle$ 11.83 $\lvert+5/2\rangle$	0.06

Table S12. The highest two m_j contributions and the 5d involvement in the major transition (states 1, 2, 9, and 10) of these four complexes are projected out, and the projection percentages are tabulated.

7. Crystal field splits for lowest 2 ground and excited SO states in Yb complexes

Index	Name of Compound	ΔE^{CF}_{ground} (meV)	$\Delta E^{CF}_{excited}$ (meV)	Reference
1	YbCp$_3$	4.60	7.60	[26]
2	K$_3$[Yb(BINOL)$_3$]	8.90	18.20	[27]
3	[Yb(DPA)$_3$]$^{3-}$	12.77	27.40	[29]
4	[Yb(S,S)-L$_3$](OTf)$_3$	13.27	17.11	[30]
5	Cs$_3$Yb$_2$Br$_9$	14.13	3.35	[31]
6	Yb^{3+} in Sr$_5$(PO$_4$)$_3$F	19.71	1.74	[32]
7	Yb^{3+} ion in Ga site in a GaN epilayer	24.80	6.57	[33]
8	Yb(C$_5$H$_7$O$_2$)$_3$	26.04	42.15	[34]
9	Cs$_2$NaYbBr$_6$	26.66	60.13	[35]
10	[Yb(Me2DO2PA)]$^+$	31.00	21.20	[29]
11	Cs$_2$NaYbCl$_6$	31.00	58.27	[35]
12	Yb(C$_{15}$H$_{11}$O$_2$)$_3$	35.46	45.13	[34]
13	[YbL1]$^{3+}$	39.05	25.66	[29]
14	Yb(C$_{10}$H$_9$O$_2$)$_3$	39.67	38.44	[34]
15	Yb(trensal)	52.90	61.00	[28]
16	(thiolfan)YbCl(THF)	66.00	78.20	[25]

Table S13. Summary of 16 different compounds.

8. Single charge fluctuation model and all-charge-moving model

The charge with the nearest atom of oxygen on THF is - 0.6152e, this charge is then assumed as the solvent effective charge, which carries much higher freedom of motion in space compared with other ligands. Once all other ligands are set to fix in space, the - 0.6152e charge is then given a freedom of motion in space, where each position is treated as a random point in space constraint in a box, the dimension of the box, $L \times L \times L$ then determines the freedom in space, 400 random points are generated in a box for a given L (to maximize the efficiency of the computing powers). For each random point, a single-point calculation using SOCF is accomplished to calculate the three transition energies corresponding to the experimentally measured three excitation bands, therefore total of 400 energies will be obtained for each band, and they analyzed using histogram with a Gaussian fit,

$$f(x) = \frac{1}{\sigma\sqrt{2\pi}} \exp\left[-\frac{(x-x_0)^2}{2\sigma^2}\right],$$ (eq. S31)

where the full width at half maximum (FWHM) is calculated as

$$FWHM = 2\sqrt{2\ln 2}\sigma.$$ (eq. S32)

In (thiolfan)YbCl(THF), the solvent coordination, THF ligand with a partial charge of -0.615e, is allowed to spatially fluctuate around its equilibrium position in a confined cubic box. The side length (L) of the box is chosen to be 0.14 Å (about 10% of the average dative bond length), 0.22 Å, 0.30 Å and 0.38 Å. In each box, 400 random positions are generated and the SOLF calculation is performed for each new configuration (Figure S8a). Figure S8b shows the three energy fluctuations associated with the excited state against the ones of the ground state while L = 0.38 Å. It can be observed that the states involved in the main absorption peak, states 1, 2, and states 9, 10 have a high correlation coefficient of 0.9997, which means that the shifts in energy associated with these states have similar responses to the solvent fluctuations.[24] Because this highly correlated energy movement greatly weakens the inhomogeneous broadening, a narrow major absorption peak is expected. While higher energy absorptions, such as the excitations to states 11, 12 or 13, 14, their energy correlations with states 1 and 2 are smaller, which indicates that they should have wider linewidth, according to the full width at half maximum (FWHM) calculation, they are roughly 7 to 8 times wider compared with the narrow peak. The histograms of transition energy are illustrated in Figure S8c, together with the absorption spectrum at room temperature, the histograms are able to well describe the general shape of the absorption spectrum.
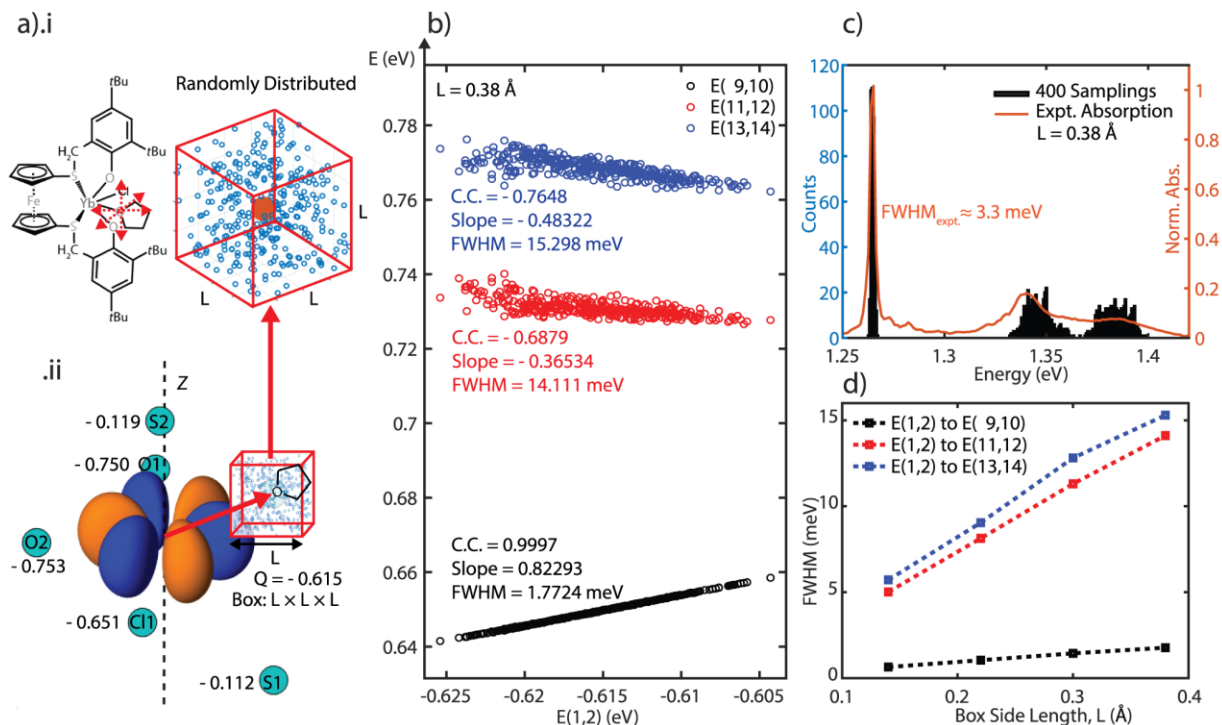

Figure S8. a. Solvent THF coordination on Yb(III) center as a movable ligand, red arrows indicate 3 spatial freedoms. The spatial orbital of ($j = 7/2, m_j = +7/2$) is used to indicate the overall spatial orientation, and the effective point charges are summarized and associated with the Yb-bonded atoms. O3 is the THF oxygen which contains a -0.615e charge and is allowed to fluctuate within a constraint (box). **b.** Correlation plot of E(9,10), E(11,12), and E(13,14) against E(1,2) of (thiolfan)YbCl(THF) with a -0.615e charge fluctuating in a cubic box (L = 0.38 Å), the energies from 400 samplings are illustrated with the correlation coefficients (C.C.), slopes of linear regression, and the FWHMs. **c.** Transition energy histograms of (thiolfan)YbCl(THF) 400 random samplings with L = 0.38 Å overlaid with the experimental absorption spectrum. **d.** FWHMs associated with each (thiolfan)YbCl(THF) f-f transition band at different single-charge fluctuation confinement sizes.

Furthermore, the linewidths of each absorption peak related to the box side length are plotted, a linear relation is observed in Figure S8d, which allows the prediction of the fluctuation scale of the narrowest ever measured 0.6 meV absorption linewidth for (thiolfan)YbCl(THF) (Shin, Zhao, Dickerson, and Shen) to be $L \sim 0.14$ Å, which can be considered as the effective solvent charge fluctuating in a cubic space with a side length of 10% of the average dative bond length.[25]

In Table S14, we present a comprehensive summary of the statistical results related to the ground energy and excited energy. It is evident that when the correlation between the excited and ground energies is exceptionally high (i.e., the energies both rise or fall simultaneously), and the linear regression slope approaches unity (indicating a similar scale of energy fluctuation), an extremely narrow absorption spectrum becomes evident.
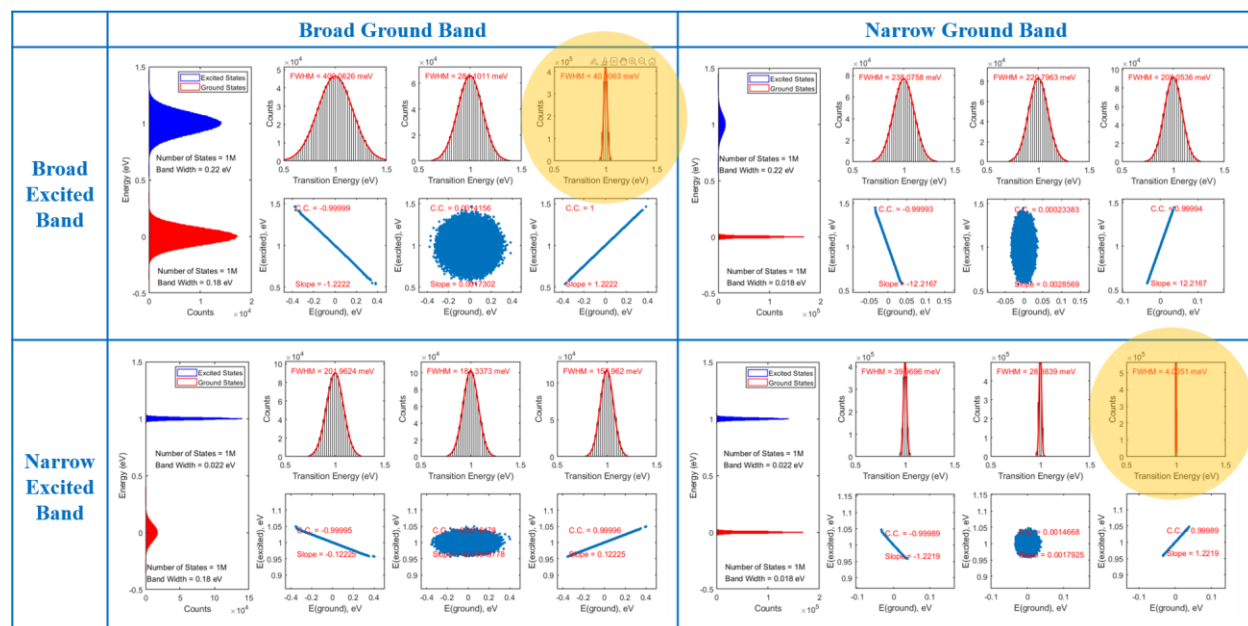

Table S14. Summary of generalized correlated fluctuation and inhomogeneous linewidth, one can see that highly correlated excited-ground state energy fluctuation is one of two key factors of narrow inhomogeneous linewidth, another key factor is the similar scale of energy fluctuations of the excited and ground states, i.e., the linear regression slope of the energy-energy correlation plot tends to 1.

In Figure S9, we show a full transition energy statistic from all-charge-moving model with two selected low-frequency vibrational modes on top of the experimental spectra for YbCp$_3$, K$_3$[Yb(BINOL)$_3$], Yb(trensal), and (thiolfan)YbCl(THF). The excited-ground energy correlation plots are illustrated next to the spectra.
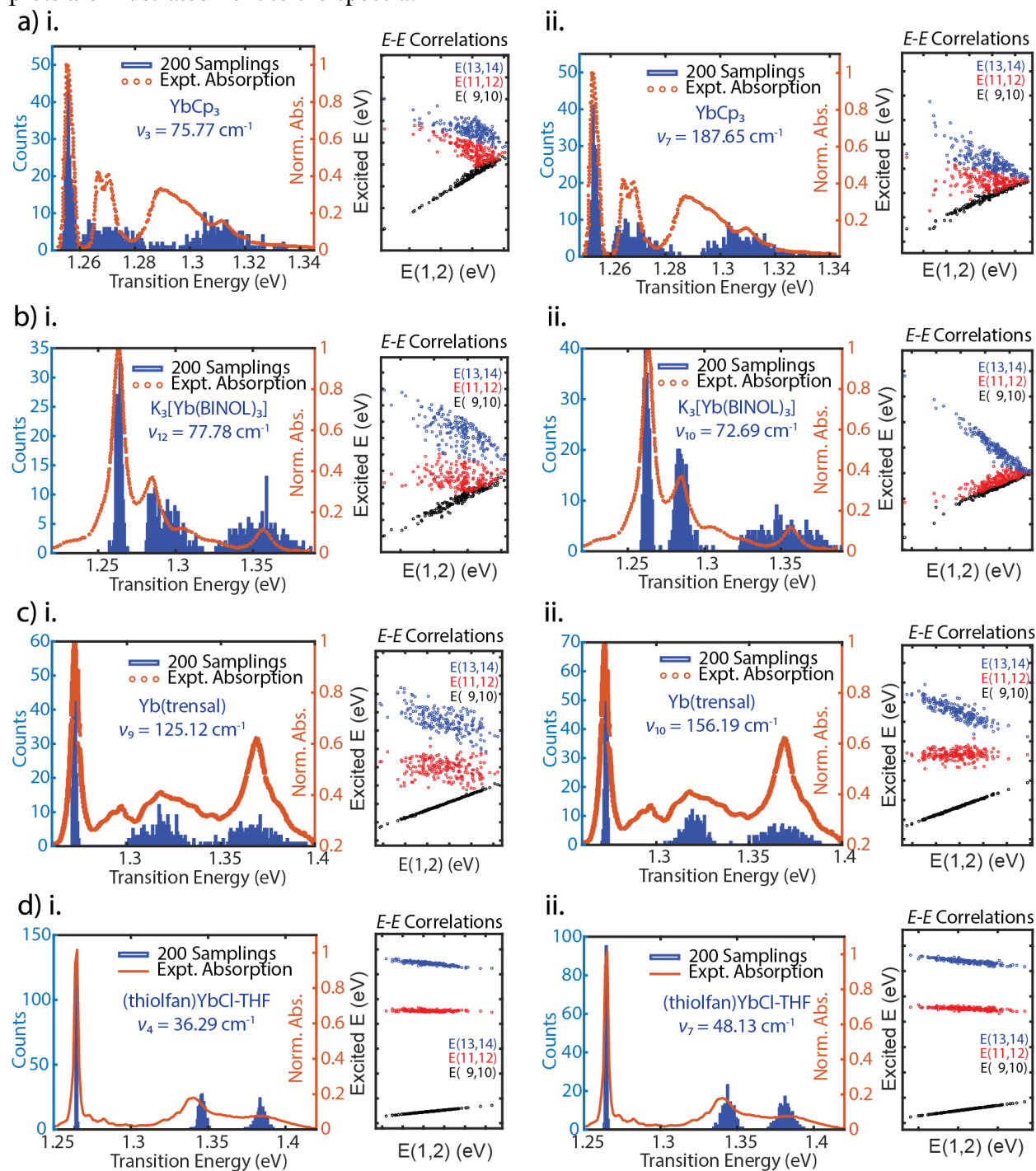

Figure S9. All-charge-moving model 200-sampling transition energy histogram overlaid with the experimental spectrum and the excited-ground energy correlation plot corresponding to the 2 selected modes, **i.** and **ii.** (as discussed in the main text) for **a.** YbCp$_3$, **b.** K$_3$[Yb(BINOL)$_3$], **c.** Yb(trensal), and **d.** (thiolfan)YbCl(THF).

VS. E(1,2)		YbCp$_3$		K$_3$[Yb(BINOL)$_3$]		Yb(trensal)		(thiolfan)YbCl	
		Mode 3	Mode 7	Mode 12	Mode 10	Mode 9	Mode 10	Mode 4	Mode 7
E(9,10)	C.C.	0.9996	0.9786	0.9616	0.9785	0.9991	0.9990	0.9991	0.9994
	Slope	0.8279	0.8509	0.9986	0.8381	0.8737	0.8646	0.8396	0.8304
	FWHM	2.8568	2.5701	4.2913	4.2845	1.6931	1.4207	0.6146	1.0458
E(11,12)	C.C.	-0.7056	-0.1326	-0.1046	0.8373	-0.1858	0.0417	-0.2461	-0.6353
	Slope	-0.2427	-0.0828	-0.0887	0.6118	-0.1648	0.0231	-0.0967	-0.2593
	FWHM	20.8317	13.7579	20.7331	9.9550	18.7167	11.3205	4.4709	8.0011
E(13,14)	C.C.	-0.9167	-0.7630	-0.6800	-0.9670	-0.6325	-0.8430	-0.8823	-0.8675
	Slope	-0.6129	-0.7741	-0.9265	-1.4686	-0.7193	-0.9014	-0.7717	-0.5962
	FWHM	26.8941	20.8657	32.6732	44.6562	24.8577	20.0215	7.0047	10.0609

Table S15. Linear correlation coefficients (C.C.) of E(9,10), E(11,12), and E(13,14) against E(1,2), linear regression slopes, and Gaussian-fitted full width at the half maximums (FWHM) in meV associated with YbCp$_3$, K$_3$[Yb(BINOL)$_3$], Yb(trensal), and (thiolfan)YbCl(THF). For each compound, two low-frequency modes are selected; in (thiolfan)YbCl(THF), modes 4 and 7 that primarily correspond to the coordinated THF fluctuation are picked; for the other compounds, one axial and one equatorial mode with respect to their principal axis are used.

References

(1) Koseki, S.; Matsunaga, N.; Asada, T.; Schmidt, M. W.; Gordon, M. S. Spin-Orbit Coupling Constants in Atoms and Ions of Transition Elements: Comparison of Effective Core Potentials, Model Core Potentials, and All-Electron Methods. *J. Phys. Chem. A* **2019**, *123* (12), 2325–2339. https://doi.org/10.1021/acs.jpca.8b09218.

(2) L. H. Thomas. The Motion of the Spinning Electron. *Nature* **1926**, *117*, 514–514.

(3) Carl J. Ballhausen. *Introduction to Ligand Field Theory* ; McGraw-Hill Book Company, Inc.: NewYork, SanFrancisco, Toronto, London, **1962**.

(4) Duan, C. K.; Tanner, P. A. What Use Are Crystal Field Parameters? A Chemist's Viewpoint. *J. Phys. Chem. A* **2010**, *114* (19), 6055–6062. https://doi.org/10.1021/jp1015214.

(5) Parker, D.; Suturina, E. A.; Kuprov, I.; Chilton, N. F. How the Ligand Field in Lanthanide Coordination Complexes Determines Magnetic Susceptibility Anisotropy, Paramagnetic NMR Shift, and Relaxation Behavior. *Acc Chem Res* **2020**, *53* (8), 1520–1534. https://doi.org/10.1021/acs.accounts.0c00275.

(6) Dun, Z.; Bai, X.; Stone, M. B.; Zhou, H.; Mourigal, M. Effective Point-Charge Analysis of Crystal Fields: Application to Rare-Earth Pyrochlores and Tripod Kagome Magnets R3Mg2Sb3O14. *Phys Rev Res* **2021**, *3* (2). https://doi.org/10.1103/PhysRevResearch.3.023012.

(7) Monteiro, B.; Coutinho, J. T.; Pereira, L. C. J. Heterometallic 3d-4f SMMs. In *Lanthanide-Based Multifunctional Materials: From OLEDs to SIMs*; Elsevier, **2018**; pp 233–261. https://doi.org/10.1016/B978-0-12-813840-3.00007-7.

(8) Carl J. Ballhausen. *Introduction to Ligand Field Theory*; McGraw-Hill Book Company, Inc.: NewYork, SanFrancisco, Toronto, London, **1962**.

(9) Atanasov, M.; Andreici Eftimie, E. L.; Avram, N. M.; Brik, M. G.; Neese, F. First-Principles Study of Optical Absorption Energies, Ligand Field and Spin-Hamiltonian Parameters of

Cr3+Ions in Emeralds. *Inorg Chem* **2022**, *61* (1), 178–192. https://doi.org/10.1021/acs.inorgchem.1c02650.

(10) Kubo, H.; Hirose, T.; Nakashima, T.; Kawai, T.; Hasegawa, J. Y.; Matsuda, K. Tuning Transition Electric and Magnetic Dipole Moments: [7]Helicenes Showing Intense Circularly Polarized Luminescence. *J. Phys. Chem. Lett.* **2021**, *12* (1), 686–695. https://doi.org/10.1021/acs.jpclett.0c03174.

(11) Sinan Karaveli; Rashid Zia. *Optical Frequency Magnetic Dipole Transitions*; Springer Netherlands, **2012**. https://doi.org/10.1007/978-90-481-9751-4.

(12) P. Lazzeretti, R. Z.; P. J. Stephens. *Magnetic Dipole Transition Moments and Rotational Strengths of Vibrational Transitions: An Alternative Formalism*; 1986; Vol. 90.

(13) T Carnall, Y. W.; Fields, P. R.; Wybourne, B. G. *Spectral Intensities of the Trivalent Lanthanides and Actinides in Solution. I*; **1965**; Vol. 42.

(14) Kolesnikov, I. E.; Mamonova, D. v.; Kurochkin, M. A.; Kolesnikov, E. Y.; Lähderanta, E. Eu3+-Doped Ratiometric Optical Thermometers: Experiment and Judd-Ofelt Modelling. *Opt Mater (Amst)* **2021**, *112*. https://doi.org/10.1016/j.optmat.2020.110797.

(15) Ćirić, A.; Stojadinović, S.; Brik, M. G.; Dramićanin, M. D. Judd-Ofelt Parametrization from Emission Spectra: The Case Study of the Eu3+ 5D1 Emitting Level. *Chem Phys* **2020**, *528*. https://doi.org/10.1016/j.chemphys.2019.110513.

(16) Ramakrishna, G.; Nagabhushana, H.; Prasad, B. D.; Vidya, Y. S.; Sharma, S. C.; Anantharaju, K. S.; Prashantha, S. C.; Choudhary, N. Spectroscopic Properties of Red Emitting Eu3+ Doped Y2SiO5 Nanophosphors for WLED′s on the Basis of Judd–Ofelt Analysis: Calotropis Gigantea Latex Mediated Synthesis. *J Lumin* **2017**, *181*, 153–163. https://doi.org/10.1016/j.jlumin.2016.08.050.

(17) Lukens, W. W.; Speldrich, M.; Yang, P.; Duignan, T. J.; Autschbach, J.; Kögerler, P. The Roles of 4f- and 5f-Orbitals in Bonding: A Magnetochemical, Crystal Field, Density Functional Theory, and Multi-Reference Wavefunction Study. *Dalton Transactions* **2016**, *45* (28), 11508–11521. https://doi.org/10.1039/c6dt00634e.

(18) Kolesnikov, I. E.; Mamonova, D. V.; Kurochkin, M. A.; Kolesnikov, E. Y.; Lähderanta, E. Eu3+-Doped Ratiometric Optical Thermometers: Experiment and Judd-Ofelt Modelling. *Opt Mater (Amst)* **2021**, *112*. https://doi.org/10.1016/j.optmat.2020.110797.

(19) Ćirić, A.; Stojadinović, S.; Brik, M. G.; Dramićanin, M. D. Judd-Ofelt Parametrization from Emission Spectra: The Case Study of the Eu3+ 5D1 Emitting Level. *Chem Phys* **2020**, *528*. https://doi.org/10.1016/j.chemphys.2019.110513.

(20) Hehlen, M. P.; Brik, M. G.; Krämer, K. W. 50th Anniversary of the Judd-Ofelt Theory: An Experimentalist's View of the Formalism and Its Application. *J Lumin* **2013**, *136*, 221–239. https://doi.org/10.1016/j.jlumin.2012.10.035.

(21) Hatanaka, M.; Yabushita, S. Theoretical Study on the F-f Transition Intensities of Lanthanide Trihalide Systems. *J. Phys. Chem. A* **2009**, *113* (45), 12615–12625. https://doi.org/10.1021/jp9049507.

(22) Tsuboi, T.; Scacco, A. *Observation of Absorption Bands Due to the 4f 7 → 4f 7 Parity-Forbidden Transitions of Eu 2+ Ions in KMgF 3 Crystals*; **1998**; Vol. 10.

(23) Feng, R.; Yu, X.; Autschbach, J. Spin-Orbit Natural Transition Orbitals and Spin-Forbidden Transitions. *J Chem Theory Comput* **2021**, *17* (12), 7531–7544. https://doi.org/10.1021/acs.jctc.1c00776.

(24) Khalil, M.; Demirdöven, N.; Tokmakoff, A. Coherent 2D IR Spectroscopy: Molecular Structure and Dynamics in Solution. *J. Phys. Chem. A* **2003**, pp 5258–5279. https://doi.org/10.1021/jp0219247.

(25) Shin, A. J.; Zhao, C.; Shen, Y.; Dickerson, C. E.; Li, B.; Bím, D.; Atallah, T. L.; Oyala, P. H.; Alson, L. K.; Alexandrova, A. N.; Diaconescu, P. L.; Campbell, W. C.; Caram, J. R. Toward Liquid Cell Quantum Sensing: Ytterbium Complexes with Ultra-Narrow Absorption. **2022**. 10.26434/chemrxiv-2022-vg4jr.

(26) Denning, R. G.; Harmer, J.; Green, J. C.; Irwin, M. Covalency in the 4f Shell of Tris-Cyclopentadienyl Ytterbium (YbCp3)-A Spectroscopic Evaluation. *J Am Chem Soc* **2011**, *133* (50), 20644–20660. https://doi.org/10.1021/ja209311g.

(27) Aspinall, H. C.; Dwyer, J. L. M.; Greeves, N.; Steiner, A. Li3[Ln(Binol)3]·6THF: New Anhydrous Lithium Lanthanide Binaptholates and Their Use in Enantioselective Alkyl Addition to Aldehydes. *Organometallics* **1999**, *18* (8), 1366–1368. https://doi.org/10.1021/om981011s.

(28) Pedersen, K. S.; Dreiser, J.; Weihe, H.; Sibille, R.; Johannesen, H. V.; Sørensen, M. A.; Nielsen, B. E.; Sigrist, M.; Mutka, H.; Rols, S.; Bendix, J.; Piligkos, S. Design of Single-Molecule Magnets: Insufficiency of the Anisotropy Barrier as the Sole Criterion. *Inorg Chem* **2015**, *54* (15), 7600–7606. https://doi.org/10.1021/acs.inorgchem.5b01209.

(29) Esteban-Gómez, D.; Büldt, L. A.; Pérez-Lourido, P.; Valencia, L.; Seitz, M.; Platas-Iglesias, C. Understanding the Optical and Magnetic Properties of Ytterbium(III) Complexes. *Inorg Chem* **2019**. https://doi.org/10.1021/acs.inorgchem.8b03354.

(30) Gendron, F.; Di Pietro, S.; Abad Galán, L.; Riobé, F.; Placide, V.; Guy, L.; Zinna, F.; Di Bari, L.; Bensalah-Ledoux, A.; Guyot, Y.; Pilet, G.; Pointillart, F.; Baguenard, B.; Guy, S.; Cador, O.; Maury, O.; Le Guennic, B. Luminescence, Chiroptical, Magnetic and: Ab Initio Crystal-Field Characterizations of an Enantiopure Helicoidal Yb(Iii) Complex. *Inorg Chem Front* **2021**, *8* (4), 914–926. https://doi.org/10.1039/d0qi01194k.

(31) Hehlen, M. P.; Güdel, H. U. Optical Spectroscopy of the Dimer System Cs3Yb 2Br9. *J Chem Phys* **1993**, *98* (3), 1768–1775. https://doi.org/10.1063/1.464265.

(32) Gruber, J. B.; Zandi, B.; Merkle, L. Crystal-Field Splitting of Energy Levels of Rare-Earth Ions Dy3+(4f9) and Yb3+(4f13) in M(II) Sites in the Fluorapatite Crystal Sr5(PO4)3F. *J Appl Phys* **1998**, *83* (2), 1009–1017. https://doi.org/10.1063/1.366790.

(33) Koubaa, T.; Dammak, M.; Kammoun, M.; Jadwisienczak, W. M.; Lozykowski, H. J. Crystal Field and Zeeman Parameters of Substitutional Yb3+ Ion in GaN. *J Alloys Compd* **2010**, *496* (1–2), 56–60. https://doi.org/10.1016/j.jallcom.2010.01.152.

(34) Peekins, W. G.; Crosby, G. A. Crystal-Field Splitting in Yb3+ Chelates. *J Chem Phys* **1965**, *42* (1), 407–414. https://doi.org/10.1063/1.1695708.

(35) Zhou, X.; Reid, M. F.; Faucher, M. D.; Tanner, P. A. Electronic Spectra of Cs2NaYbF6 and Crystal Field Analyses of YbX63- (X = F, Cl, Br). *J. Phys. Chem. B* **2006**, *110* (30), 14939–14942. https://doi.org/10.1021/jp057241j.